




RESEARCH ARTICLE

Heavy macrophage infiltration identified by optical coherence tomography relates to plaque rupture

Xuan Shi^{1,*} , Tao Tao^{2,*}, Yi Wang², Yunfei Han¹, Xiaohui Xu¹, Qin Yin¹, Fang Wang¹, Rui Liu¹  & Xinfeng Liu^{1,3} 

¹Department of Neurology, Nanjing Jinling Hospital, Affiliated Hospital of Medical School, Nanjing University, Nanjing, China

²Department of Neurosurgery, Nanjing Drum Tower Hospital, Affiliated Hospital of Medical School, Nanjing University, Nanjing, China

³Stroke Center and Department of Neurology, First Affiliated Hospital of University of Science and Technology of China, Division of Life Sciences and Medicine, University of Science and Technology of China, Hefei, China

Correspondence

Xinfeng Liu and Rui Liu, Department of Neurology, Nanjing Jinling Hospital, Affiliated Hospital of Medical School, Nanjing University, 305 East Zhongshan Rd, Nanjing 210002, China. Tel +86 2584801861; Fax +86 2584805169; E-mail: xfliu2@vip.163.com (X. L.) and E-mail: liurui8616@163.com (R. L.)

Received: 1 July 2023; Revised: 31 August 2023; Accepted: 2 October 2023

Annals of Clinical and Translational Neurology 2023; 10(12): 2334–2346

doi: 10.1002/acn3.51923

*These authors contributed equally to this work.

Abstract

Objective: Risk stratification plays a critical role in patients with asymptomatic carotid atherosclerotic stenosis. Heavy macrophage infiltration (HMC) is an important factor of plaque destabilization. However, in vivo imaging technologies and screening criteria for HMC remain limited. We aimed to (i) introduce algorithms for in vivo detection of macrophage infiltrations using optical coherence tomography (OCT) and (ii) to investigate the threshold of HMC and its association with plaque vulnerability. **Methods:** Ex vivo OCT images were co-registered with histopathology in 282 cross-sectional pairs from 19 carotid endarterectomy specimens. Of these, 197 randomly selected pairs were employed to define the parameters, and the remaining 85 pairs were used to evaluate the accuracy of the OCT-based algorithm in detecting macrophage infiltrations. Clinical analysis included 93 patients receiving carotid OCT evaluation. The prevalence and burden of macrophage infiltration were analyzed. Multivariable and subgroup analysis were performed to investigate the association between HMC and plaque rupture. **Results:** The sensitivity and specificity of algorithm for detecting macrophage infiltration were 88.0% and 74.9%, respectively. Of 93 clinical patients, ruptured plaques exhibited higher prevalence of macrophage infiltration than nonruptured plaques (83.7% [36/43] vs 32.0% [16/50], $p < 0.001$). HMC was identified when the macrophage index was greater than 60.2 (sensitivity = 74.4%, specificity = 84.0%). Multivariable analysis showed that HMC and multiple calcification were independent risk factors for non-lipid-rich plaque rupture. **Interpretation:** This study provides a novel approach and screening criteria for HMC, which might be valuable for atherosclerotic risk stratification.

Introduction

Carotid atherosclerotic stenosis remains an important cause of ischemic stroke. About 10%–15% of all first ever stroke patients will have an unheralded ischemic stroke from a previously untreated asymptomatic carotid artery stenosis.^{1,2} The current treatment of patients with asymptomatic carotid atherosclerotic stenosis is based on the degree of stenosis.³ However, asymptomatic patients with high-risk plaques had significantly higher risk of ipsilateral ischemic cerebrovascular events than those without

high-risk plaques with similar degrees of stenosis.⁴ In this context, risk stratification of carotid atherosclerotic plaques becomes critical. Macrophage infiltration (MC) plays a pivotal role in both atherogenesis and destabilization of carotid plaques.⁵ Histopathological study has shown that the abundance of MC is associated with higher predicted stroke risk.^{6,7} The assessment of the intraplaque MC burden seems inseparable from risk stratification of carotid atherosclerotic plaques. Nevertheless, current imaging technologies of in vivo identify heavy macrophage infiltrations (HMC) remain limited. Traditional imaging

modalities such as ultrasound, multidetector-row CT angiography, and MR angiography, with the aid of contrast enhancement, could provide indications of the presence of MC by revealing plaque enhancement. However, their specificity is somewhat constrained.⁸ Recently, ¹⁸F-fluorodeoxyglucose PET/CT and PET/MR have displayed potential in detecting active inflammation within plaques,^{7,9} but they are incapable of evaluating vascular anatomy, plaque composition, and additional morphological characteristics.

Optical coherence tomography (OCT), a real-time intravascular imaging technique with ultra-high resolution, can assist in assessing the microarchitecture of vessels, including vasa vasorum, cholesterol crystals, erosion, and more.^{10–12} In the last decade, studies performed by OCT have allowed us to shed new light on the pathologic substrate of cerebrovascular disease.^{13–15} What's more, MC could be visible on OCT images as signal-rich, distinct, or confluent punctate regions that exceed the intensity of background speckle noise.¹⁶ The overall superiority of OCT provides us with a reliable imaging tool to screen for HMC and help achieve plaque risk stratification. Therefore, the purpose of this study was two-fold: (i) to introduce and validate a set of OCT-based algorithms for automatic assessment of MC and (ii) to determine the threshold of HMC and certify the association between HMC and plaque rupture (PR).

Material and Methods

Study design

The focus of this study was two-fold: (i) histological validation of OCT-based automatic MC identification algorithms (OCT-MCI) in carotid endarterectomy (CEA) specimens; (ii) quantitative assessment of MC in vivo in human, and exploration the risk threshold of HMC and its association with PR (Fig. 1). This study was approved by the Ethics Committee of Jinling Hospital and Nanjing Drum Tower Hospital. Written informed consent was obtained from all patients prior to CEA and/or OCT assessment.

CEA specimens

Nineteen specimens from patients who underwent CEA for severe ($\geq 70\%$) atherosclerotic internal carotid artery stenosis were collected between June 2019 and June 2021 in the Department of Neurosurgery at Nanjing Drum Tower Hospital. OCT examinations were conducted within 72 hours postoperatively. Following OCT image acquisition as described below, the specimens were pressure-fixed by formalin and decalcified with

ethylenediaminetetraacetic acid to maintain their orientation and size for comparison with OCT images.^{17,18} These specimens were serially sectioned to the longitudinal axis of the vessel at 1-mm block. From the distal side of each 1-mm block, histopathology slides of 4- μ m at 16- μ m intervals were prepared. Slides were serially selected at 0.1-mm intervals and stained with HE and Movat pentachrome, respectively. Each histopathology slide was digitized using a microscope at low magnification ($\times 1.25$) and scanned using the 3D Panoramic Viewer system when necessary.

Patients in the clinical study

We conducted a retrospective review of cases that underwent OCT examination of the internal carotid artery at Jinling Hospital from January 2017 to June 2022. The inclusion criteria were as follows: 1) the presence of an atherosclerotic stenosis lesion; and 2) the target vessel had not undergone endovascular treatment (balloon dilation or stenting) or endarterectomy before OCT examination. The exclusion criteria consisted of nonanalyzable images, which were defined as such if more than 3/4 of target segment could not be visualized due to serious artifact or intraluminal blood.¹⁹ A total of 102 cases met the inclusion criteria, of which nine cases were classified as having nonanalyzable images. Ultimately, 93 cases were included in the clinical study. Baseline information and clinical data of patients during hospitalization were collected and recorded, including age, gender, history of hypertension, diabetes, coronary heart disease, stroke, current smoking, and alcohol consumption, as well as biochemical parameters.

OCT image acquisition

OCT images were acquired using a frequency domain OCT system (ILUMEN OPTIS System or C7-XR, St. Jude Medical, USA) and a 2.7-F Dragonfly OCT Imaging Catheter (C7 Dragonfly Catheter or Dragonfly Duo Catheter, St. Jude Medical, USA). In the histopathology study, the OCT imaging catheter was guided by a guidewire through the CEA specimen (Fig. S1). After the images were calibrated for Z-bias, an automatic retraction at a speed of 25 mm/s was performed to obtain a serial set of OCT images. In the clinical study, the OCT imaging catheter was delivered distal to the stenotic lesion in the internal carotid artery under the guidance of a 0.3556 mm (0.014 in) PT microwire (Fig. S1). Images were acquired by injecting 20 ml of 100% contrast medium at a flow rate of 10 ml/s through the guiding catheter to flush out the blood, with the pressure set at 200 psi (pounds per square inch, 1 psi = 6.895 kPa). Calibration was completed, and

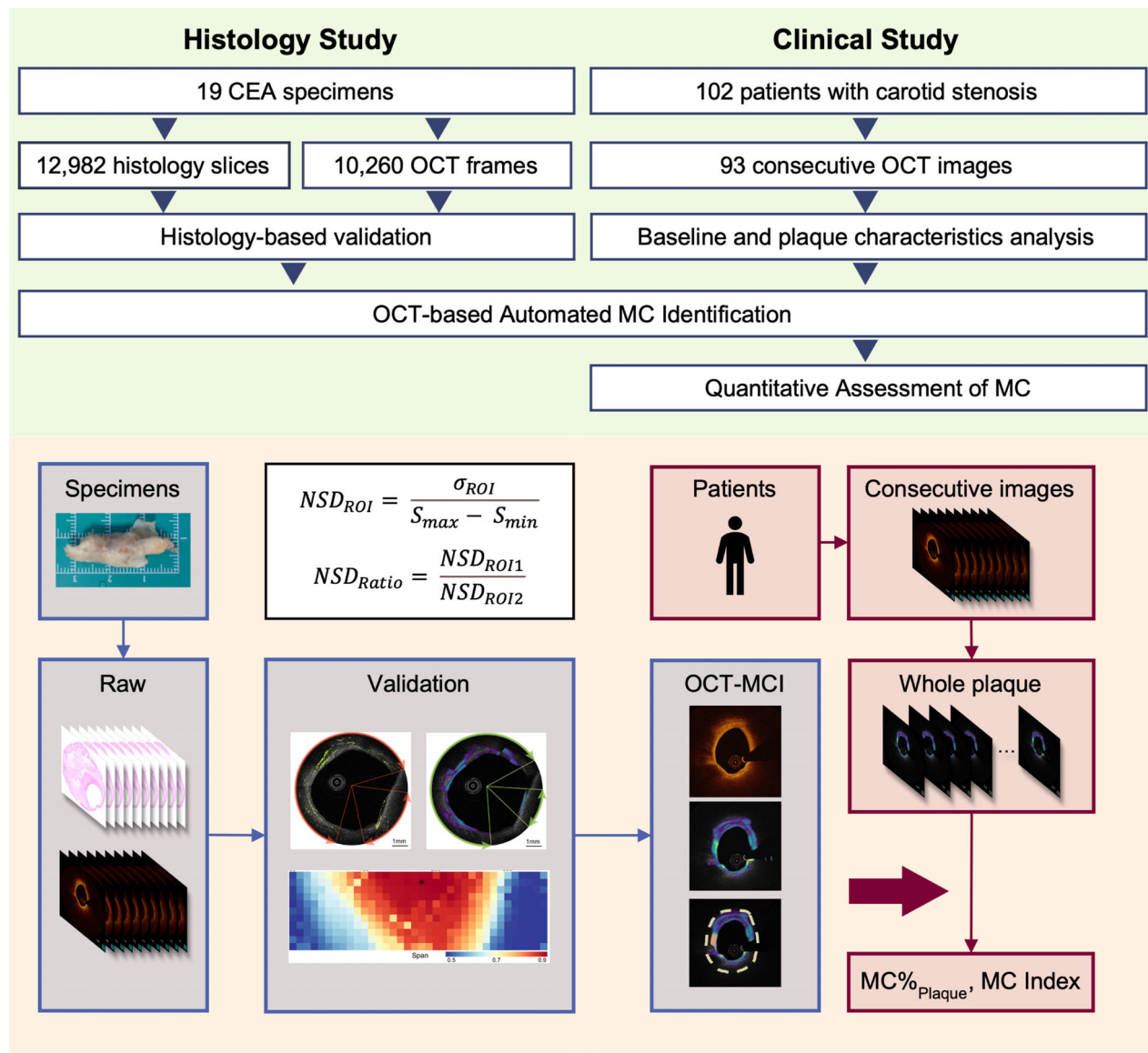


Figure 1. Study design. CEA, carotid endarterectomy. MC, macrophage infiltration. OCT, optical coherence tomography. OCT-MCI, OCT-based automatic MC identification algorithms.

images were obtained after an automatic retraction. All images were stored in digital format using proprietary software (St. Jude Medical, USA) for subsequent offline analysis.

OCT image analysis

OCT images were independently analyzed by two experienced OCT investigators who were blinded to the clinical data. In cases where there was disagreement between the two results, re-evaluation was performed by a third OCT investigator, and the result was recorded after consensus

was reached by all three. Lipid plaque was defined as a diffusely bordered signal-poor region with an overlying signal-rich band. Lipid-rich plaque was identified if the arc of $>90^\circ$ within a plaque. PR was characterized by the discontinuity of the fibrous cap or/and cavitation within the plaque. Calcification was defined as an area with low backscattering signal and a sharp border inside of a plaque.²⁰ The number of calcifications within each plaque was recorded, and they were then divided into single and multiple calcifications. Thrombus appeared as a backscattering floating in or protruding into the carotid lumen with a dimension of at least 250 μm . Neovascularization

was defined as signal-absent holes within a plaque between 50 and 300 μm in diameter, and visible for at least three consecutive frames on pullback imaging.¹⁰ Cholesterol crystals were defined as thin linear structures with high signal and low signal attenuation.¹²

OCT and histology co-registration

A total of 12,982 histopathology slides were obtained, and image matching was achieved by one OCT investigator and one pathology investigator. The thickness of each histology slice was 4 μm with a 16 μm interval between two slices. The thickness of each OCT cross-sectional frame was 100 μm , allowing for approximately 5 histological slices per 1 OCT frame. The electronic histological images were first sequentially picked out at 1-mm interval (about 50 slices, 10 OCT cross-sectional frames). Preliminary pairing of histological images with OCT images was performed according to the site of carotid bifurcation, the size and morphology of the lumen contour, and the characteristics of the plaque, to roughly confirm the matching range and serial number.¹⁸ Subsequently, secondary exact matching was performed at 0.1-mm intervals (approximately 5 slices, 1 OCT cross-sectional frames). The matched group was defined as an OCT cross-sectional frame and several pairing histological slices. Finally, there were 1559 matched groups, which included 1559 OCT cross-sectional frames and 6951 histological slices. Considering potential morphological and compositional similarities between two consecutive OCT frames, the matched groups were selected sequentially at 0.5-mm intervals (5 OCT cross-sectional frames). For each matched group, one slice with the best lumen morphology was chosen for CD 68 immunohistochemical staining. Slices were electronically stored using the 3D Panoramic Viewer system. In the end, a total of 311 pairs of 1:1 matched OCT images and CD 68 immunohistochemical stained histology images were obtained.

Considering the inevitable extrusion and deformation during specimen sectioning, the “Big Wrap” plug-in in Fiji software was used for image registration.²¹ The “Color Deconvolution” function and “Threshold (auto-set)” function of Fiji software were utilized to extract the CD 68 + regions of each slice. If the CD 68 + region was less than 0.5%, the slice was considered to have no MC region. Thus, a total of 282 matched pairs were included in the analysis. The extracted CD 68 + region was then assigned to the matched OCT image in the same proportion to obtain the histology-based classification images (Fig. S2). According to these histology-based classification images, the accuracy of OCT-MCI classification was tested by computational binary vector methods (Supplementary Methods).

From the 282 pairs of histopathological cross section and corresponding OCT image, 197 pairs were randomly selected for a training dataset and used to investigate the best thresholds of parameters in the OCT-MCI. Subsequently, the remaining 85 pairs were used as testing dataset. The OCT-MCI algorithm whose parameters were determined based on the training dataset was prospectively applied for the testing dataset.

OCT-based MC identification

Python 3.10 software was used for OCT image preprocessing and MC identification. The main objectives of OCT raw image preprocessing were to improve image quality and automatically extract the effective-analyzed regions (ER). Speckle noise reduction was performed using median filtering, mean filtering, Gaussian filtering, and bilateral filtering. The effect of speckle noise removal was evaluated by contrast to noise ratio and equivalent number of looks, with bilateral filtering showing the best results. Dynamic programming (DP) was utilized for catheter guidewire removal and automatic identification of lumen boundaries. To ensure the accuracy and repeatability of the algorithm in identifying lumen boundaries, dice similarity coefficient (DSC) and Jaccard coefficient were used to compare manual segmentation results by OCT researchers and automatic segmentation results by the algorithm.

DSC is used to measure the similarity of a set, and a higher value represents a higher similarity of the set.²²

$$DSC(A, M) = \frac{2|A \cap M|}{|A| + |M|}$$

Jaccard is used to evaluate the similarity and difference between the two datasets.²³

$$Jaccard(A, M) = \frac{|A \cap M|}{|A \cup M|}$$

Fifteen pullbacks were randomly chosen from the OCT image dataset, and 150 images (10 frames per pullback) were randomly selected. Lumen boundaries were manually delineated by two independent OCT investigators for each image set. The results indicated that the agreement between Investigator 1 and Investigator 2 was high, and their respective results were highly correlated with the results of DP algorithm (Table S1). Therefore, the DP algorithm was determined to be an effective algorithm for vessel lumen detection. Considering the penetration depth of the OCT itself around 1–1.3 mm, the ER of the carotid OCT images was defined as the region where the identified lumen boundaries expand 1 mm outward.

Within the ER of each cross-sectional frame, the resulting OCT raw-intensity image was normalized from 0 to

1. The normalized standard deviation (NSD) was calculated by applying a standard deviation spatial filter:

$$NSD_{ROI} = \frac{\sigma_{ROI}}{S_{max} - S_{min}}$$

$$\sigma_{ROI}^2 = \frac{1}{N-1} \sum_x \sum_y (S(x, y) - \bar{S})^2; S(x, y) \in ROI$$

where S_{max} and S_{min} are the maximum and minimum intensity values of the ER, N is the total number of the pixels in the region of interest (ROI), $S(x, y)$ is the OCT sign as a function of x and y locations within the ROI, and \bar{S} is the mean value of the OCT signal within the ROI.^{24,25} Normalized standard deviation ratio (NSDR) was calculated as the ratio of NSD values of the pixel (ROI1, punctuated signal-rich areas) and the pixel located at a predefined span deeper in the axial direction (ROI2, signal-attenuated areas or shadows).²⁶ The NSDR value was computed as

$$NSD_{Ratio} = \frac{NSD_{ROI1}}{NSD_{ROI2}}$$

The optimal parameter values of ROI's span and ROI's size were determined in the histology-based training dataset. The performance of the algorithm was evaluated in the histology-based testing dataset.

OCT-based MC quantitative evaluation

A series of consecutive OCT cross-sectional images acquired from one case was performed for automated quantitative assessment of MC. Based on the prevalence of MC, the case was classified as having or not having MC. The total number of MC-identified frames was recorded. The longitudinal length of MC was defined as OCT frame thickness multiplied by the total number of MC-identified frames. The algorithm automatically calculated the MC burden (MC%_{slice}) for each frame, and outputted the mean MC burden (MC%_{plaque}) and maximum MC burden (MC%_{Max}) for each plaque. The MC index for each plaque was obtained by multiplying the mean MC%_{plaque} and the longitudinal length. A receiver operating characteristic curve (ROC) was performed to determine the threshold of the MC index for predicting PR. Then, HMC was defined as plaques with an MC index larger than this threshold.

Statistical analysis

Clinical statistical analyses were carried out using IBM SPSS 23.0 software (IBM, Armonk, NY) and R version 4.2.3 (R Development Core Team, Vienna, Austria). Categorical variables were presented as frequencies (percentages) and compared between groups using the chi-square test or Fisher's exact test. The distribution of continuous

variables was tested by the Kolmogorov–Smirnov test. Continuous variables with normal distribution were described as mean \pm SD, and comparisons were performed using an independent samples t-test. Variables with skewed distribution were described as median (the 25th to the 75th percentile), and comparisons were performed using Mann–Whitney U-test. Interobserver and intra-observer reliability was assessed using Cohen Kappa test for categorical variables and intraclass correlation test for continuous variables.

ROC analysis was utilized to determine the best cutoff value of MC index of each plaque to predict PR. Interaction terms were used to explore whether the association between HMC and PR differed according to MLA, lipid-rich plaque, cholesterol crystal, and calcification. A p -value of less than 0.05 was regarded as indicating interaction on the multiplicative scale. The relative excess risk due to interaction (RERI), attributable proportion due to interaction (AP), the synergy index (S), and corresponding 95% confidence intervals were employed as measures of additive interaction. Multivariate analysis was conducted to assess the independent impact of HMC on PR within non-lipid-rich plaques by adjusting for variables including MLA <9.36, with cholesterol crystals and with multiple calcifications. The significance level was set to $p < 0.05$, and all tests of hypotheses were 2-sided.

Results

Parameter optimization and performance of OCT-based MC identification

In the examination of the histological training dataset, the accuracy of the OCT-MCI, measured by the area under the curve area (AUC), varied depending on the size and span of the ROI (Fig. 2). The maximum AUC of 0.928 was achieved when the ROI size was 21 pixels and the ROI span was 230 pixels. The accuracy, sensitivity, and specificity for OCT of identifying MC was 89.0%, 95.6%, and 80.9%, respectively. Subsequently, the performance of the algorithm was evaluated in the histological testing dataset. As a result, with histology as the gold standard, the accuracy of the OCT-MCI was 82.3%, with sensitivity of 88.0% and specificity of 74.9%.

MC and plaque characteristics

In the clinical analysis, out of 93 carotid atherosclerotic stenotic lesions, 55.9% (52/93) of plaques were detected with MC by OCT-MCI. Analysis of plaque type via OCT revealed that plaques with MC were more frequently classified as lipid-rich plaques (67.3% [35/52] vs 4.9% [2/41], $p < 0.001$; Table 1). Compared to plaques without MC,

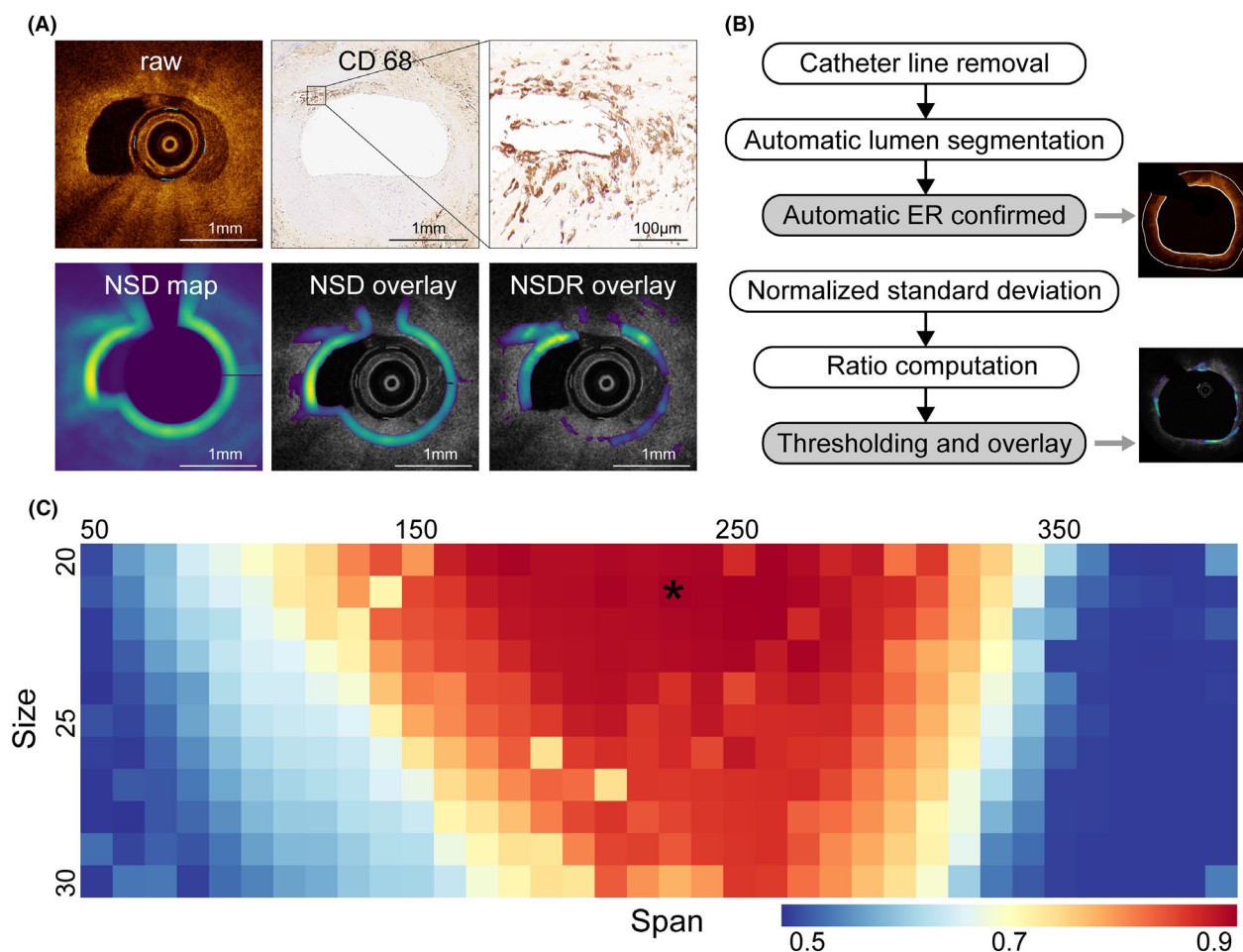


Figure 2. (A) Representative case of OCT-based automatic MC detection. (B) Steps of OCT-based automated MC analysis. (C) ROC-AUC value as a function of ROI size and span for the NSDR-based classification. The asterisk mark indicates optimal ROI size (21 pixels) and span (230 pixels) values that led to the highest ROC-AUC value. ER, effective-analyzable region; NSD, normalized standard deviation; NSDR, normalized standard deviation ratio.

those with MC had a smaller minimal luminal area (8.2 ± 4.7 vs 10.9 ± 6.9 , $p = 0.04$) and a higher prevalence of PR (69.2% [36/52] vs 17.1% [7/41], $p < 0.001$). Detailed characteristics were assessed between the two groups. Cholesterol crystals were more commonly detected in plaques with MC (36.5% [19/52] vs 14.6% [6/41], $p = 0.02$). In contrast, neovascularization (17.3% [9/52] vs 14.6% [6/41], $p = 0.73$), intraluminal thrombus (19.2% [10/52] vs 12.2% [5/41], $p = 0.36$), and calcifications (44.2% [23/52] vs 29.3% [12/41], $p = 0.14$) were not significantly different between plaques with or without MC.

Association between MC and PR

Of 93 atherosclerotic stenotic lesions in the clinical study, 46.2% (43/93) of plaques were detected with fibrous cap

disruption through OCT (Table 2). Among them, 83.7% (36/43) of ruptured plaques were detected with MC by the algorithm, whereas only 32.0% (16/50) of nonruptured plaques had MC. In the ruptured plaques, the MC index was significantly higher than in the nonruptured plaques (125.2 [55.5–199.4] vs 0 [0–50.0], $p < 0.001$). The mean $MC\%_{\text{plaque}}$ (19.6 [14.3–23.6] vs 0 [0–11.3], $p < 0.001$) and longitudinal length (6.0 [3.5–9.4] vs 0 [0–2.1], $p < 0.001$) were also higher in ruptured plaques compared to nonruptured plaques. The ROC curve was utilized to determine the threshold of MC index for predicting PR. The Youden index was largest when the MC index was 60.2, with the AUC of 0.85, sensitivity of 74.4%, and specificity of 84.0%. Based on the cutoff value of MC index (> 60.2), 40 plaques were classified as HMC plaques. Of these, 80% (32/40) of HMC plaques were combined with fibrous cap disruption, while only 16%

	Patients with MC (n = 52)	Patients without MC (n = 41)	p value
Demographic characteristics			
Age, years	68 (61–72)	66 (58–69)	0.13
Male sex, n (%)	18 (34.6)	16 (40.0)	0.60
Body mass index, kg/m ²	25.1 ± 3.1	25.0 ± 2.7	0.81
Clinical features, n (%)			
Hypertension	41 (78.8)	32 (80.0)	0.89
Diabetes mellitus	20 (58.8)	14 (41.2)	0.73
Prior stroke/TIA	16 (30.8)	12 (30.0)	0.94
Coronary heart disease	15 (28.8)	9 (22.5)	0.49
Current smoking	21 (40.4)	15 (37.5)	0.78
Biochemical parameters			
Triglycerides, mmol/L	1.4 (1.0–2.0)	1.2 (1.1–1.7)	0.63
Total cholesterol, mmol/L	3.4 (2.9–4.3)	3.5 (2.8–4.1)	0.91
HDL, mmol/L	1.0 (0.9–1.1)	1.0 (0.9–1.1)	0.50
LDL, mmol/L	1.8 (1.5–2.4)	2.0 (1.4–2.4)	0.68
Creatinine, μmol/L	66.0 (55.9–78.8)	60.6 (55.8–70.2)	0.09
Serum glucose, mmol/L	5.6 (4.8–7.1)	5.4 (4.9–6.3)	0.33
OCT findings			
MLA, mm ²	8.2 ± 4.7	10.9 ± 6.9	0.04
Plaque rupture, n (%)	36 (69.2)	7 (17.1)	<0.001
Lipid-rich plaque, n (%)	35 (67.3)	2 (4.9)	<0.001
Thrombus, n (%)	10 (19.2)	5 (12.2)	0.36
Cholesterol crystals, n (%)	19 (36.5)	6 (14.6)	0.02
Neovascularization, n (%)	9 (17.3)	6 (14.6)	0.73
Calcifications, n (%)	23 (44.2)	12 (29.3)	0.14
Multiple calcifications, n (%)	12 (23.1)	6 (14.6)	0.31

HDL, high-density lipoprotein; LDL, low-density lipoprotein; MC, macrophage infiltrations; MLA, minimum luminal area; TIA, transient ischemic attack.

Table 1. Comparison of clinical characteristic and OCT findings based on the presence of MC detected by OCT-MCI.

(8/43) of nonruptured plaques exhibited HMCs ($p < 0.001$). Additionally, compared to nonruptured plaques, ruptured plaques had a larger lipid core (69.8% [30/50] vs 14.0% [7/43], $p < 0.001$), a higher prevalence of thrombus (30.2% [13/50] vs 4.0% [2/43], $p = 0.001$), and multiple calcifications (32.6% [14/50] vs 8.0% [4/43], $p = 0.003$).

Association between HMC and PR: subgroup analysis

Subgroup analyses were conducted based on plaque characteristics to further investigate the association between HMC and PR (Fig. 3). Subgroup analyses were based on the full data set in the clinical study. HMC was shown to be a risk factor for PR after adjusting for lipid-rich plaques (adjusted odds ratio [OR], 6.34 [95% CI 1.93–20.85]). Subgroup analysis showed no significant statistical association between HMC and PR in lipid-rich plaques (OR, 0.83 [95% CI 0.08–8.52]; $p = 0.88$). However, HMC remained a risk factor for PR in non-lipid-rich plaques (OR, 23.92 [95% CI 3.99–143.22]; $p = 0.003$). There

was a multiplicative interaction between lipid-rich plaques and HMC ($p = 0.03$), but not additive interaction (RERI, −28.61 [95% CI −118.51 – 61.28]; AP, −1.00 [95% CI −4.41 – 2.40]; S, 0.49 [95% CI 0.09–2.78]). In the other subgroups, both overall and subgroup analyses showed that HMC represented as a risk factor for PR, including MLA, cholesterol crystals, and calcifications, and none of interactions were found.

Association between HMC and PR in non-lipid-rich plaques

In the clinical analysis, variables that were found to be statistically different between ruptured plaques and non-ruptured plaques in the univariate analysis, including MLA (<9.36), cholesterol crystals, multiple calcifications, and HMC, were included in the multivariate model (Fig. 4). The multivariate analysis revealed that HMC (OR, 54.15 [95% CI 5.98–490.15]; $p < 0.001$) and multiple calcifications (OR, 17.72 [95% CI 1.89–165.77]; $p = 0.01$) were independently associated with non-lipid-rich plaque rupture, whereas MLA (<9.36) and

Table 2. Comparison of clinical characteristics, MC features, and OCT finding based on the presence of plaque rupture.

	Patients with PR (n = 43)	Patients without PR (n = 50)	p value
Demographic characteristics			
Age, years	67 (61–70)	66 (60–70)	0.45
Male sex, n (%)	28 (65.1%)	30 (61.2)	0.70
Body mass index, kg/m ²	25.1 ± 3.0	25.0 ± 2.9	0.87
Systolic blood pressure, mmHg	140.6 ± 19.7	136.2 ± 16.5	0.25
Diastolic blood pressure, mmHg	78 (72–86)	77 (69–80)	0.16
Clinical features, n (%)			
Hypertension	32 (74.4)	41 (83.7)	0.27
Diabetes mellitus	17 (39.5)	17 (34.7)	0.63
Prior stroke/TIA	12 (27.9)	16 (32.7)	0.62
Coronary heart disease	14 (32.6)	10 (20.4)	0.19
Current smoking	17 (39.5)	19 (38.8)	0.94
Biochemical parameters			
Triglycerides, mmol/L	1.4 (1.1–1.9)	1.1 (1.0–1.8)	0.11
Total cholesterol, mmol/L	3.5 (2.9–4.5)	3.5 (2.8–4.0)	0.36
HDL, mmol/L	1.0 ± 0.2	1.0 ± 0.2	0.75
LDL, mmol/L	1.8 (1.5–2.4)	1.9 (1.5–2.5)	0.69
Creatinine, μmol/L	64.0 (54.0–74.2)	65.5 (57.3–77.2)	0.58
Serum glucose, mmol/L	5.6 (4.9–7.0)	5.5 (4.8–6.4)	0.54
MC features			
With MC, n (%)	36 (83.7)	16 (32.0)	<0.001
Longitudinal length, mm	6.0 (3.5–9.4)	0 (0–2.1)	<0.001
Maximum area, %	27.3 (17.9–34.0)	0 (0–15.0)	<0.001
Mean area, %	19.6 (14.3–23.6)	0 (0–11.3)	<0.001
MC index	125.2 (55.5–199.4)	0 (0–50.0)	<0.001
HMC, n (%)	32 (74.4)	8 (16.0)	<0.001
OCT findings			
MLA, mm ²	8.0 ± 5.7	10.5 ± 5.9	0.04
Lipid-rich plaque, n (%)	30 (69.8)	7 (14.0)	< 0.001
Thrombus, n (%)	13 (30.2)	2 (4.0)	0.001
Cholesterol crystals, n (%)	14 (32.6)	11 (22.0)	0.25
Neovascularization, n (%)	8 (18.6)	7 (14.0)	0.55
Calcifications, n (%)	24 (55.8)	11 (22.0)	0.001
Multiple calcifications, n (%)	14 (32.6)	4 (8.0)	0.003

HDL, high-density lipoprotein; LDL, low-density lipoprotein; MC, macrophage infiltrations; MLA, minimum luminal area; PR, plaque rupture; TIA, transient ischemic attack.

cholesterol crystals were not significant. This suggested that HMC represented as an independent risk factor for fibrous cap disruption in non-lipid-rich plaques after adjusting for multiple associated factors.

Discussion

The main findings of this study were as follows: (1) OCT-based algorithms for automatic MC identification *in vivo* were introduced. The sensitivity and specificity of OCT-MCI for detecting MC were 88.0% and 74.9%, respectively. (2) MC was identified in 83.7% of ruptured plaques. The burden of MC, calculated as MC index, was significantly higher in ruptured plaques than in

nonruptured plaques. (3) HMC was identified as an independent risk factor for PR in non-lipid-rich plaques.

In this study, an algorithm was established for OCT-based automatic MC identification *in vivo* using open-source Python language. Previous study by Tearney's team showed a correlation between punctuated signal-rich bright spots on OCT images and the presence of MC in fibrous cap of fibroatheromas plaques, and introduced NSD as an imaging marker for MC identification.²⁴ NSD was then used to identify MC in preselected regions on OCT, which were mainly within fibrous cap or plaque shoulder.^{25,27,28} Researchers have compared the effectiveness of MC identification based on three different parameters: NSD, granulometry index, and signal attenuation,

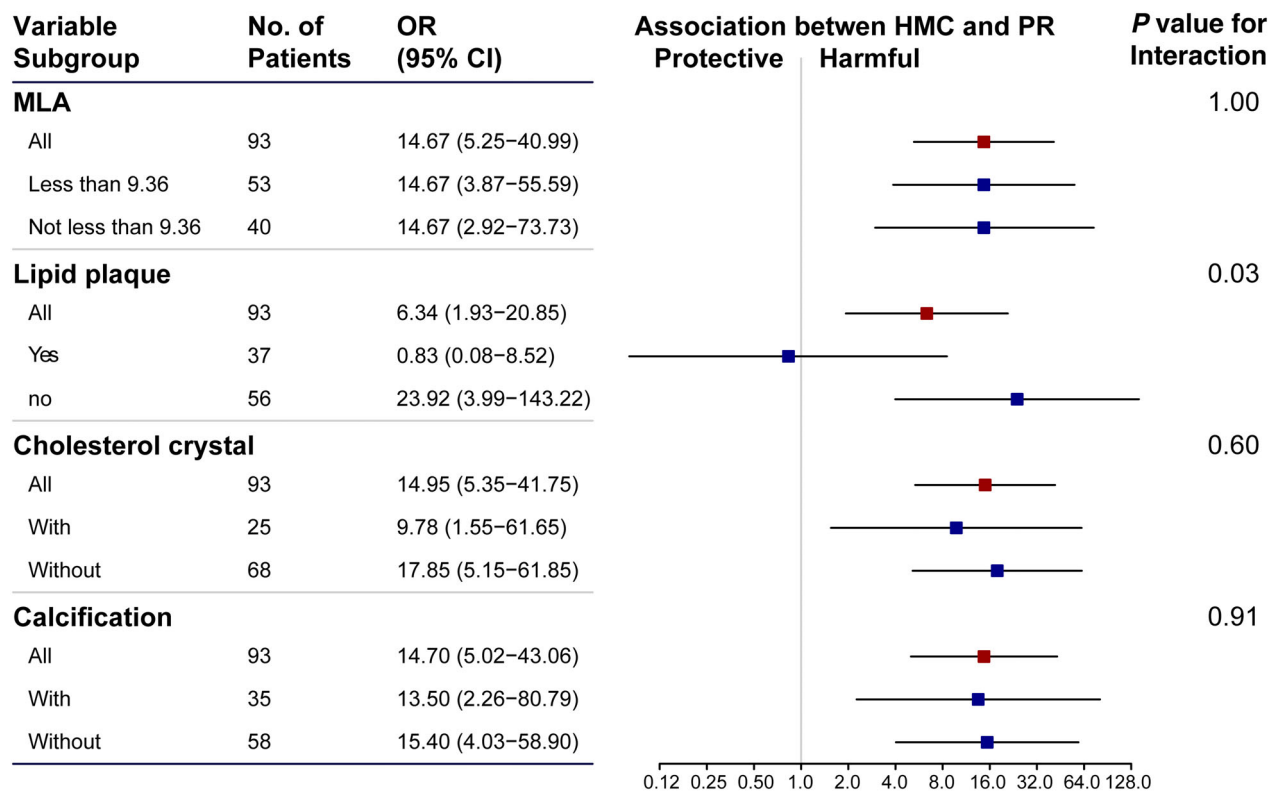


Figure 3. Subgroup analyses. HMC was shown to be a risk factor for PR after adjusting for lipid-rich plaques. No significant statistical association was found between HMC and PR in lipid-rich plaques. However, HMC remained a risk factor for PR in non-lipid-rich plaques. In the other subgroups, both overall and subgroup analyses showed that HMC represented as a risk factor for PR, including MLA, cholesterol crystals, and calcifications, and none of interactions were found. CI, confidence interval; HMC, heavy macrophage infiltration; MLA, minimum lumen area; OR, odds ratio.

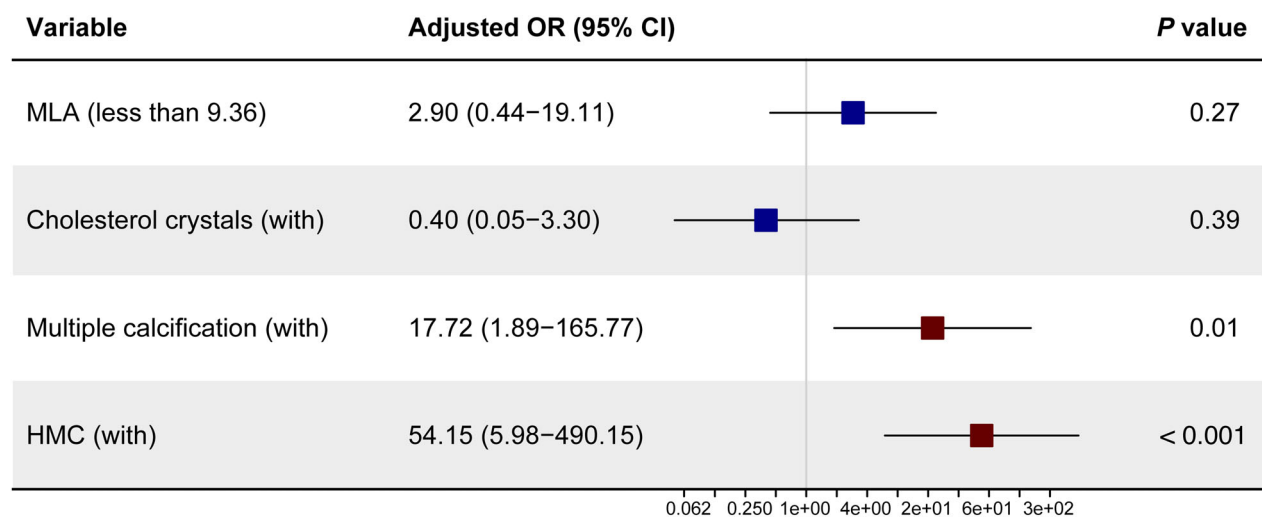


Figure 4. Multivariable logistic regression analysis for plaque rupture. HMC and multiple calcifications were independently associated with non-lipid-rich plaque rupture, whereas MLA (<9.36) and cholesterol crystals were not significant. CI, confidence interval; HMC, heavy macrophage infiltration; MLA, minimum lumen area; OR, odds ratio.

and found that NSD analysis exhibited the highest accuracy.²⁷ However, other plaque components such as the external elastic lamina and plaque healing could also produce high NSD values.²⁹ Recently, Javier's team proposed an improved method based on NSD analysis by adding the ratio processing of punctuated signal-rich areas (with high NSD values) to signal-attenuated areas or shadows (with low NSD values) in a subsequently deeper axial region, which led to significant improvements in the accuracy, specificity, and sensitivity of NSD-based recognition.²⁶

The study has made several improvements by incorporating the concept of NSDR and utilizing the characteristics of cerebrovascular OCT images. Firstly, filter preprocessing was employed to improve the image quality for the inherent speckle on OCT images. Secondly, unlike previous investigations conducted on coronary arteries, the penetration depth of OCT in carotid plaques is limited, which poses challenges in accurately defining the analyzable range of images during manual reading in clinical settings. To mitigate excessive analysis and minimize errors in manual readings, ER was used to quantitatively evaluate MC in carotid plaques. Although the whole-plaque macrophage density rarely exceeds a few percent,^{5,30} the superficial macrophage density is usually high.³¹ Thus, the MC% calculated based on ER may better reflect the clinical focus and provide clinicians with reference values. In the future, combining OCT with imaging techniques that offer improved penetration, such as intravascular ultrasound, may enable more comprehensive evaluation of deeper plaques structure.

In the present study, HMC was identified as an independent risk factor for PR in non-lipid-rich plaques. This suggests that even in plaques lacking a lipid-rich core, HMC may pose a threat to plaque homeostasis by degrading the collagen-rich cap matrix and inhibiting new collagen synthesis.^{32,33} This discovery introduces a novel finding that the presence of HMC could serve as a crucial indicator of atherosclerosis progression in non-lipid-rich plaques. While initial ruptures in this type of plaques may be healed and clinically silent, persistent HMC not only triggers further inflammation but also contributes to the re-rupture of the fibrous cap.³⁴ Such *de novo* ruptures, compared to first-time ruptures, are more likely to generate artery-to-artery embolisms or result in severe stenosis, ultimately leading to stroke.^{35,36} Conversely, there was no significant independent association found between HMC and PR in lipid-rich plaques. We hypothesized that lipid-rich plaques might require reaching a relatively higher risk threshold to disrupt the initial temporary equilibrium within the plaque. Future studies with larger sample sizes are necessary to validate this hypothesis. Nevertheless, in lipid-rich plaques, sustained

HMC also contributes to increased inflammation, which subsequently leads to rupture and thrombosis.⁵ Although the timing and mechanism of rupture may differ between HMC plaques with and without large lipid cores, persistent HMC remains a significant trigger that jeopardizes plaque homeostasis. Therefore, early consideration of aggressive management might be recommended once HMC is detected, regardless of whether patients have lipid-rich plaques or not. For instance, promoting anti-inflammatory diets in the daily health management of these patients could be beneficial, as studies have indicated that such diets may be associated with reduced plaque vulnerability and vascular events.^{37,38} Additionally, more intensive cholesterol lowering therapy or the addition of anti-inflammatory agents may need to be considered.

More importantly, our findings may inspire the design of forthcoming clinical trials aimed at risk stratification for identifying patients at increased risk of stroke while undergoing medical therapy. Growing evidence suggests that stroke could be attributed to the presence of vulnerable plaques, even in the absence of moderate or severe stenosis.^{4,7,39–41} As medical therapy advances and risk factor control improves, the benefits of surgery or stenting may diminish.^{42,43} Hence, it becomes imperative to identify patients with asymptomatic carotid stenosis with stable and with unstable plaques and to select those patients who would benefit from carotid intervention. A recent study has indicated that persistent increasing active inflammation may hinder plaques from exhibiting a favorable response and rendering them vulnerable despite statin therapy. This is evident by the development of new layered plaques, which undergo a cycle of rupture and healing, ultimately contributing to plaque progression.⁴⁴ Incorporating plaque inflammation into current selection strategies may target patients who are most likely to derive long-term benefits from carotid revascularization, both in the early and late stages. However, the limited methods available for assessing MC hinder further analysis regarding the extent of MC that would benefit most from carotid revascularization. Our exploratory study introduces a novel approach for quantifying MC and initially determines the risk threshold of HMC based on a limited number of clinical samples. This may provide a valuable reference for designing future trials that investigate risk models enriched with imaging data.

Over the past decade, OCT has emerged as a promising technology for cerebrovascular assessment, offering enhanced possibilities for detailed evaluation of both extracranial and intracranial vessels.^{13,45,46} Due to its high resolution, OCT holds the potential to serve as an effective tool for precision medicine, including automatic image recognition and machine learning.^{47,48} However,

commercially available OCT imaging catheters were primarily designed for coronary arteries, which imposes certain limitations when employed in cerebrovascular assessment. Firstly, when assessing middle cerebral arteries with tortuous pathways, the imaging catheter may be vulnerable to damage caused by excessive tortuosity.⁴⁹ Fortunately, this limitation appears to be circumvented when evaluating extracranial vessels and vertebrobasilar arteries that exhibit relatively straight pathways. Furthermore, the depth of penetration of OCT imaging catheters remains limited in cerebrovascular assessment. This hinders their capacity to assess deeper structures and vascular remodeling. In the future, this challenge could be addressed by incorporating intravascular ultrasound assessment, which offers greater depth of penetration. Overall, it seems imperative to develop OCT imaging catheters specifically tailored for cerebrovascular assessment.

This study has some limitations. Firstly, the resolution of OCT imaging limited the identification of specific subtypes of inflammatory cells in the OCT image-based algorithm. However, this limitation could potentially be addressed in the future through the implementation of high-frequency OCT or micro-OCT.⁵⁰ Secondly, the algorithm has not yet been able to analyze lesions of in-stent neo-atherosclerosis due to the high signal emitted by the stent wire within plaques, which might cause errors. Lastly, the sample size for the clinical analysis remains limited. Future studies with larger sample sizes may provide more robust data to support the findings of this study.

Conclusively, this study introduced an OCT-based algorithm for automatic assessment of MC *in vivo*. HMC (MC index >60.2) identified by the algorithm was an independent risk factor for PR even in non-lipid-rich plaques. This study provides a novel approach for *in vivo* identification of MC and new screening criteria for HMC plaques, which might be valuable for early detection and monitoring of high-risk atherosclerotic plaques.

Acknowledgements

This project was supported by National Natural Science Foundation of China (81530038, 81901218), and National Key Research and Development Program of China (2017YFC1307901).

Author Contributions

Conceptualization: Xinfeng Liu, Rui Liu, Xuan Shi, and Tao Tao; Methodology: Yi Wang, Yunfei Han, Qin Yin, and Rui Liu; Formal analysis and investigation: Xuan Shi, Tao Tao, Xiaohui Xu, Fang Wang, and Rui Liu; Writing

—original draft preparation: Xuan Shi and Tao Tao; Writing—review and editing: Rui Liu; Funding acquisition: Xinfeng Liu and Rui Liu; Supervision: Xinfeng Liu.

Conflict of interest

The authors declare that there is no conflict of interest.

Data Availability Statement

Data that support the findings of this study are available for sharing with qualified investigators on reasonable request.

References

1. Naylor AR. Why is the management of asymptomatic carotid disease so controversial? *Surgeon*. 2015;13:34-43.
2. Hogberg D. Asymptomatic carotid stenosis: the silent threat. *Eur J Vasc Endovasc Surg*. 2021;61:374.
3. Abbott AL, Paraskevas KI, Kakkos SK, et al. Systematic review of guidelines for the management of asymptomatic and symptomatic carotid stenosis. *Stroke*. 2015;46:3288-3301.
4. Kamtchum-Tatuene J, Noubiap JJ, Wilman AH, Saqqur M, Shuaib A, Jickling GC. Prevalence of high-risk plaques and risk of stroke in patients with asymptomatic carotid stenosis: a meta-analysis. *JAMA Neurol*. 2020;77:1524-1535.
5. Bentzon JF, Otsuka F, Virmani R, Falk E. Mechanisms of plaque formation and rupture. *Circ Res*. 2014;114:1852-1866.
6. Howard DP, van Lammeren GW, Rothwell PM, et al. Symptomatic carotid atherosclerotic disease: correlations between plaque composition and ipsilateral stroke risk. *Stroke*. 2015;46:182-189.
7. McCabe JJ, Camps-Renom P, Giannotti N, et al. Carotid plaque inflammation imaged by pet and prediction of recurrent stroke at 5 years. *Neurology*. 2021;97:e2282-e2291.
8. Brinjikji W, Huston J 3rd, Rabinstein AA, et al. Contemporary carotid imaging: from degree of stenosis to plaque vulnerability. *J Neurosurg*. 2016;124:27-42.
9. Robson PM, Kaufman A, Pruzan A, et al. Scan-rescan measurement repeatability of (18)f-fdg pet/mr imaging of vascular inflammation. *J Nucl Cardiol*. 2022;29:1660-1670.
10. Li L, Dmytriw AA, Krings T, Feng Y, Jiao L. Visualization of the human intracranial vasa vasorum *in vivo* using optical coherence tomography. *JAMA Neurol*. 2020;77:903-905.
11. Montone RA, Vetrugno V, Camilli M, et al. Macrophage infiltrates in coronary plaque erosion and cardiovascular outcome in patients with acute coronary syndrome. *Atherosclerosis*. 2020;311:158-166.

12. Shi X, Cai H, Wang F, et al. Cholesterol crystals are associated with carotid plaque vulnerability: an optical coherence tomography study. *J Stroke Cerebrovasc Dis*. 2020;29:104579.
13. Xu X, Li M, Liu R, et al. Optical coherence tomography evaluation of vertebrobasilar artery stenosis: case series and literature review. *J Neurointerv Surg*. 2020;12:809-813.
14. Xu X, Huang FH, Shi X, et al. Optical coherence tomography evaluation of carotid artery stenosis and stenting in patients with previous cervical radiotherapy. *Front Neuroscience*. 2022;16:861511.
15. Xu R, Yang B, Li L, et al. Macrocalcification of intracranial vertebral artery may be related to in-stent restenosis: lessons learned from optical coherence tomography. *J Neurointerv Surg*. 2021;14:475-479.
16. Tearney GJ, Regar E, Akasaka T, et al. Consensus standards for acquisition, measurement, and reporting of intravascular optical coherence tomography studies: a report from the international working group for intravascular optical coherence tomography standardization and validation. *J Am Coll Cardiol*. 2012;59:1058-1072.
17. Prabhudesai V, Phelan C, Yang Y, Wang RK, Cowling MG. The potential role of optical coherence tomography in the evaluation of vulnerable carotid atheromatous plaques: a pilot study. *Cardiovasc Intervent Radiol*. 2006;29:1039-1045.
18. Shimokado A, Matsuo Y, Kubo T, et al. In vivo optical coherence tomography imaging and histopathology of healed coronary plaques. *Atherosclerosis*. 2018;275:35-42.
19. Liu R, Jiang Y, Xiong Y, et al. An optical coherence tomography assessment of stent strut apposition based on the presence of lipid-rich plaque in the carotid artery. *J Endovasc Ther*. 2015;22:942-949.
20. Nakajima A, Araki M, Kurihara O, et al. Predictors for rapid progression of coronary calcification: an optical coherence tomography study. *J Am Heart Assoc*. 2021;10:e019235.
21. John A, Bogovic PH, Wong A, Stephan Saalfeld. Robust Registration of Calcium Images by Learned Contrast Synthesis. *IEEE*; 2015.
22. Ughi GJ, Verjans J, Fard AM, et al. Dual modality intravascular optical coherence tomography (oct) and near-infrared fluorescence (nirf) imaging: a fully automated algorithm for the distance-calibration of nirf signal intensity for quantitative molecular imaging. *Int J Cardiovasc Imaging*. 2015;31:259-268.
23. Miyagawa M, Costa MGF, Gutierrez MA, Costa JPGF, Filho CFFC. Lumen segmentation in optical coherence tomography images using convolutional neural network. *Annu Int Conf IEEE Eng Med Biol Soc*. 2018;2018:600-603.
24. Tearney GJ. Quantification of macrophage content in atherosclerotic plaques by optical coherence tomography. *Circulation*. 2002;107:113-119.
25. MacNeill BD, Jang IK, Bouma BE, et al. Focal and multifocal plaque macrophage distributions in patients with acute and stable presentations of coronary artery disease. *J Am Coll Cardiol*. 2004;44:972-979.
26. Rico-Jimenez JJ, Campos-Delgado DU, Buja LM, Vela D, Jo JA. Intravascular optical coherence tomography method for automated detection of macrophage infiltration within atherosclerotic coronary plaques. *Atherosclerosis*. 2019;290:94-102.
27. Di Vito L, Agozzino M, Marco V, et al. Identification and quantification of macrophage presence in coronary atherosclerotic plaques by optical coherence tomography. *Eur Heart J Cardiovasc Imaging*. 2015;16:807-813.
28. Scalone G, Niccoli G, Refaat H, et al. Not all plaque ruptures are born equal: an optical coherence tomography study. *Eur Heart J Cardiovasc Imaging*. 2017;18:1271-1277.
29. Phipps JE, Vela D, Hoyt T, et al. Macrophages and intravascular oct bright spots: a quantitative study. *JACC Cardiovasc Imaging*. 2015;8:63-72.
30. Falk E. Pathogenesis of atherosclerosis. *J Am Coll Cardiol*. 2006;47:C7-C12.
31. Kolodgie FD, Burke AP, Farb A, et al. The thin-cap fibroatheroma: a type of vulnerable plaque: the major precursor lesion to acute coronary syndromes. *Curr Opin Cardiol*. 2001;16:285-292.
32. Gough PJ. Macrophage expression of active mmp-9 induces acute plaque disruption in apoe-deficient mice. *J Clin Invest*. 2005;116:59-69.
33. Virmani R, Burke AP, Farb A, Kolodgie FD. Pathology of the vulnerable plaque. *J Am Coll Cardiol*. 2006;47:C13-C18.
34. Russo M, Kim HO, Kurihara O, et al. Characteristics of non-culprit plaques in acute coronary syndrome patients with layered culprit plaque. *Eur Heart J Cardiovasc Imaging*. 2020;21:1421-1430.
35. Burke AP, Kolodgie FD, Farb A, et al. Healed plaque ruptures and sudden coronary death. *Circulation*. 2001;103:934-940.
36. Kramer MC, Rittersma SZ, de Winter RJ, et al. Relationship of thrombus healing to underlying plaque morphology in sudden coronary death. *J Am Coll Cardiol*. 2010;55:122-132.
37. Peng M, Wang L, Xia Y, et al. High dietary inflammatory index is associated with increased plaque vulnerability of carotid in patients with ischemic stroke. *Stroke*. 2020;51:2983-2989.
38. Estruch R, Ros E, Salas-Salvado J, et al. Primary prevention of cardiovascular disease with a mediterranean diet supplemented with extra-virgin olive oil or nuts. *N Engl J Med*. 2018;378:e34.

39. Takaya N, Yuan C, Chu B, et al. Association between carotid plaque characteristics and subsequent ischemic cerebrovascular events: a prospective assessment with mri—initial results. *Stroke*. 2006;37:818-823.
40. Zhao X, Hippe DS, Li R, et al. Prevalence and characteristics of carotid artery high-risk atherosclerotic plaques in chinese patients with cerebrovascular symptoms: a chinese atherosclerosis risk evaluation ii study. *J Am Heart Assoc*. 2017;6:6.
41. Yamada K, Kawasaki M, Yoshimura S, et al. High-intensity signal in carotid plaque on routine 3d-tof-mra is a risk factor of ischemic stroke. *Cerebrovasc Dis*. 2016;41:13-18.
42. Reiff T, Eckstein HH, Mansmann U, et al. Carotid endarterectomy or stenting or best medical treatment alone for moderate-to-severe asymptomatic carotid artery stenosis: 5-year results of a multicentre, randomised controlled trial. *Lancet Neurol*. 2022;21:877-888.
43. Keyhani S, Cheng EM, Hoggatt KJ, et al. Comparative effectiveness of carotid endarterectomy vs initial medical therapy in patients with asymptomatic carotid stenosis. *JAMA Neurol*. 2020;77:1110-1121.
44. Nakajima A, Minami Y, Araki M, et al. Optical coherence tomography predictors for a favorable vascular response to statin therapy. *J Am Heart Assoc*. 2020;10:e018205.
45. Li T, Xu R, Ma Y, Wang T, Yang B, Jiao L. Calcification is a risk factor for intracranial in-stent restenosis: an optical coherence tomography study. *J Neurointerv Surg*. 2023;jnis-2023-020624. Epub ahead of print. doi: [10.1136/jnis-2023-020624](https://doi.org/10.1136/jnis-2023-020624)
46. Funatsu N, Enomoto Y, Egashira Y, et al. Tissue protrusion with attenuation is associated with ischemic brain lesions after carotid artery stenting. *Stroke*. 2020;51:327-330.
47. Park S, Araki M, Nakajima A, et al. Enhanced diagnosis of plaque erosion by deep learning in patients with acute coronary syndromes. *JACC Cardiovasc Interv*. 2022;15:2020-2031.
48. Shibutani H, Fujii K, Shirakawa M, et al. Diagnostic accuracy of optical frequency domain imaging for identifying necrotic cores with intraplaque hemorrhage in advanced human carotid plaques. *Am J Cardiol*. 2021;156:123-128.
49. Lopes DK, Johnson AK. Evaluation of cerebral artery perforators and the pipeline embolization device using optical coherence tomography. *J Neurointerv Surg*. 2012;4:291-294.
50. Ughi GJ, Marosfoi MG, King RM, et al. A neurovascular high-frequency optical coherence tomography system enables in situ cerebrovascular volumetric microscopy. *Nat Commun*. 2020;11:3851.

Supporting Information

Additional supporting information may be found online in the Supporting Information section at the end of the article.

Appendix S1.